Journal of the European Ceramic Society 45 (2025) 116879

Contents lists available at ScienceDirect

Journal of the European Ceramic Society

journal homepage: www.elsevier.com/locate/jeurceramsoc

Ultrafast high-temperature sintering of yttria-stabilized zirconia in reactive N_2 atmosphere

Levent Karacasulu [a,b,*], Thomas Hérisson de Beauvoir [c,**], Emanuele De Bona [a], Michele Cassetta [a], Cekdar Vakifahmetoglu [b], Vincenzo M. Sglavo [a,e], Mauro Bortolotti [a], Charles Manière [d], Claude Estournès [c], Mattia Biesuz [a,e]

[a] Department of Industrial Engineering, University of Trento, Via Sommarive 9, Trento 38123, Italy
[b] Department of Materials Science and Engineering, Izmir Institute of Technology, İzmir 35430, Türkiye
[c] CIRIMAT, CNRS-INP-UPS, Université Toulouse 3 – Paul Sabatier, 118 route de Narbonne, Toulouse 31062, France
[d] Normandie Univ, ENSICAEN, UNICAEN, CNRS, CRISMAT, Caen 14000, France
[e] INSTM, Trento Research Unit, Via G. Giusti 9, Firenze 50121, Italy

ARTICLE INFO

Keywords:
Ultrafast high-temperature sintering
Zirconia
Sintering
Solid solutions

ABSTRACT

So far, ultrafast high-temperature sintering (UHS) has always been carried out in an inert environment. In the present work, we investigated UHS of 3YSZ in nitrogen and argon atmosphere showing that "*the atmosphere matters*". Highly densified samples can be obtained in both environments but densification and grain growth are significantly retarded in N_2. Moreover, the phase evolution is strongly atmosphere-dependent with the samples treated in Ar remaining tetragonal and those treated under N_2 progressively reducing their tetragonality, eventually converting into cubic zirconia and rock salt oxynitride. The results can be explained by the incorporation of nitrogen within the ZrO_2 lattice. Electrochemical impedance spectroscopy demonstrates that while the ionic bulk conductivity are marginally influenced by the sintering atmosphere, the grain boundaries' capacitive behavior strongly changes. After UHS under 30 A, excellent ionic conductors were obtained without substantial grain boundary-blocking effects.

1. Introduction

In the decades, different non-conventional sintering strategies that induce densification of ceramic materials with limited grain growth have been introduced [1–6]. Despite they are based on different approaches to enhance densification (electric fields and currents [7,8], electromagnetic radiations [9], solvent [6,10], pressure [11]), most of them share a common feature: they allow rapid hating of the ceramic body. Examples include microwave sintering [12], fast firing [13], spark plasma sintering [2], blacklight sintering [14], ultrafast high-temperature sintering [15], and flash sintering [16,17].

Among these, ultrafast high-temperature sintering (UHS), introduced by Wang et al. in 2020 [15], has garnered particular interest. UHS enables the densification of monolithic ceramics by radiative heating (10^3-10^4 K min^{-1}) under an inert atmosphere, like argon, in extremely short times (≈ 10–300 s). To achieve this, the green body is placed within graphite felt which is quickly Joule-heated by an electrical current flow [15,18–31]. In addition, simultaneous solid-state synthesis and sintering are possible in UHS using a mixture of different ceramic powders as precursors [15,27,28,31,32–34]. UHS also aids the carbothermal reaction due to the presence of carbon felt in contact with the oxide sample at high temperatures (>1800°C) combined with an inert atmosphere [35]. Therefore, blackening observed in previous works could result from the carbothermal reaction promoted upon UHS as well as possible carbon contaminations [26,35,36].

Due to its mechanical, thermal, and electrochemical properties, doped zirconia is used in a wide range of applications, such as cutting tools, dental implants, oxygen sensors, solid oxide fuel cells, and thermal barrier coatings [21,37]. Pure zirconia possesses three polymorphs stable at different temperatures: monoclinic (T < 1170 °C), tetragonal (1170 < T < 2370 °C), and cubic (T > 2370 °C). The latter possesses the highest ionic conductivity and is employed in electrochemical devices,

* Corresponding author at: Department of Industrial Engineering, University of Trento, Via Sommarive 9, Trento 38123, Italy.
** Corresponding author.
E-mail addresses: leventkaracasulu@iyte.edu.tr, leventkaracasulu@gmail.com (L. Karacasulu), thomas.herisson-de-beauvoir@univ-tlse3.fr (T. Hérisson de Beauvoir).

https://doi.org/10.1016/j.jeurceramsoc.2024.116879
Received 22 February 2024; Received in revised form 22 August 2024; Accepted 29 August 2024
Available online 30 August 2024

whereas the tetragonal phase is used for structural applications due to its high fracture toughness [21,38].

The stabilization of the cubic and tetragonal polymorphs at room temperature is usually achieved by doping with bivalent (CaO and MgO) or trivalent oxides (Y_2O_3, Sc_2O_3, and Yb_2O_3) [21,38]. Also, anion doping is a practical approach to stabilize the high-temperature polymorphs [39–41]. For instance, zirconia hot-pressed in N_2 atmosphere shows partial substitution of nitrogen (N^{3-}) for oxygen ions (O^{2-}) [38,42]. Besides hot pressing, nitridation of zirconia was observed in various heat treatments [39,40,43,44–47], microwave plasma processing [48], laser processing [49] and flash sintering [50] under a controlled atmosphere.

UHS has already been applied to YSZ [21,35]; nevertheless, the process was carried out in an inert Ar atmosphere, with no substantial reaction with the oxide. Besides the N-doping effect on phase stability, the sintering atmosphere can also impact the densification process and microstructure evolution, resulting in variable concentration, type, and mobility of both ionic and electronic defects [51–54].

Although reactive UHS was studied using solid precursors, it has not been applied to obtain reactions or doping from a gas phase, as for zirconia sintered under N_2. The present work aims to answer the following questions: "*Does UHS in N_2 impact the phase stability of sintered YSZ artifact? Does the atmosphere affect the microstructural evolution of YSZ?*". For this reason, the simultaneous sintering and nitridation of 3 mol% yttria-stabilized zirconia (3YSZ) upon UHS under N_2 atmosphere were explored here and the obtained materials were compared with those produced by more "conventional" UHS carried out in Ar.

2. Experimental procedure

3YSZ granulated (3 % grades binder) ready-to-press commercial powder (TZ-3YSB-E, Tosoh Corporation, Tokyo, Japan) was used in this work. Cylindrical pellets, 8 mm in diameter, were obtained by uniaxial pressing (300 MPa). Before UHS, the samples were debinded at 500°C in static air for 30 min. The relative density of the green body was about 50 % after debinding (measured with a caliper, sensitivity 0.01 mm, and an analytical scale, sensitivity 0.1 mg).

For the UHS process, a carbon felt (SGL Carbon Co., Germany) with 19x70x6 mm^3 (nominal thickness 5 mm, measured thickness ≈6 mm) was clamped between two steel electrodes, resulting in an electrode span of 30 mm and a cross-section of 19×6 mm^2. The green pellets were introduced into the carbon felt through a small hole produced using a spatula on the felt side. The hole was closed with a felt fragment to prevent thermal gradients and reduce heat losses. UHS was carried out in a borosilicate flask filled with nitrogen or argon (99.999 % purity) for "reactive" and "conventional" experiments, respectively. An electric current was applied to the felt using DC power supply (Agilent Technologies, model 6674 A, Santa Clara, CA, USA), the power source always worked in current control. Different currents were applied, ranging from 15 A up to 35 A, for different holding times (1–3 min). The power dissipation under the different currents is reported in Table S1. No statistically significant differences can be observed between the two atmospheres.

In order to estimate the process temperature in the UHS system, finite element modeling (FEM) simulations were performed using COMSOL Multiphysics software. The electrothermal properties of the felt were determined by testing the heating under different imposed currents and with materials of varying melting points. The resistivity and its temperature dependence were calibrated by simulating the voltage drop profile for each imposed current, both before and after the materials reached their melting points. Details about the calibration procedures and boundary conditions used for FEM are available in the reference [30], with the validation data provided in the supplementary materials. This model has also been successfully applied for higher temperatures, as detailed in reference [29], providing a reasonable estimation of the melting point of boron carbide. Two different approaches were used to simulate the quality of the felt aperture: the "contactless" and "full contact" configurations. The "full contact" configuration assumes ideal contact with the sample and no convective heat losses on the felt inner surfaces, while the "contactless" configuration incorporates the calibrated convective losses from inside the felt. The actual temperature is expected to be closer to the "contactless" configuration, which aligns with the calibration setup. However, depending on the quality of the felt closure, the heating can be higher and approach the "full contact" configuration, especially at high current densities where radiation is dominant.

The density of the samples was determined using Archimedes' principle in a water medium at 25°C using an analytical balance with 0.1 mg sensitivity. The relative density was calculated based on a theoretical density of 3-YSZ equal to (6.05 g cm^{-3}) [55].

The polished cross-sections of samples produced under currents exceeding 30 A were thermally etched by performing a UHS under a relatively low current (24 A) for 30 s under the same atmosphere used for the original consolidation (Ar or N_2). The samples sintered at lower currents (< 30 A) were thermally etched in a conventional furnace at 950°C for 30 min to avoid possible further densification. The cross-sections were observed by SEM (SUPRA V40, Carl-Zeiss, Germany) after being coated with Pt/Pd. Grain size measurements were carried out using the linear intercept method.

X-ray diffraction was carried out on the surface of the samples using an Italstructures IPD3000 diffractometer, with copper anode source (λ = 1.5406 Å, 40 kV, 30 mA) coupled to a collimating Goebel mirror on the primary beam side and a Dectris Mythen 1 K detector on the diffracted beam side; Rietveld analysis was performed using the Maud software [56] by refining phase scale factors as well as lattice and average domain size parameters.

Raman measurements were carried out at room temperature using a micro-Raman spectrometer (Horiba Jobin-Yvon LabRam HR 800) on the external surface of the UHS samples. The exciting radiation was provided by a He-Ne laser (λ_{exc} = 632.8 nm) operating at 6 mW with a spot size of about 1.5 μm. A narrow-band notch filter was used to cut the signal from the Rayleigh line to 200 cm^{-1}. The scattered radiation was filtered by using a grating with 600 lines mm^{-1}, and detected by a nitrogen-cooled CCD detector (1024×256 pixels).

Electrical Impedance Spectroscopy (EIS) measurements were performed in air using a Frequency Response Analyzer (MTZ35, Biologic, France) at 100 mV in the frequency range of 10–10^6 Hz. The obtained data were fitted using ZView software considering an equivalent circuit consisting of R-CPEs (Resistance-Fixed Phase Elements) connected in series. Fittings lead to the adjustment of three parameters per R-CPE element, R, Q and n. These values were used to calculate the conductivity as $\sigma = t/RA$, t and A being the sample's thickness and surface area; the capacitance was obtained as $C = Q^{1/n} \; R^{(1-n)/n}$ and $f = (2\pi RC)^{-1}$. Pt sputtered layers on the polished surfaces of the specimen were used as electrodes.

X-ray Photoelectron Spectroscopy (XPS) was carried out on a Kα Thermo Scientific Spectrometer using an Al-Kα radiation. Angle-resolved measurements were performed at take-off angle $\theta = 90°$ (e.g., normal to the sample surface). Before the analysis, the samples were ionically etched to remove surface contaminations. For the survey spectra, pass energy was fixed at 160 eV and at 40 eV for high-resolution spectra. The background was calculated using the Shirley method and peaks were fitted using a Gaussian shape. A flood gun was also applied to avoid charge effects.

3. Results

The relative density evolution of 3YSZ is reported in Fig. 1**(a)** as a function of the UHS current and atmosphere. The density increases with the applied current, reflecting the higher temperature achieved by the ceramic body, which exceeds 2000°C in the case of treatments under currents above 32.5 A. FEM simulations point out that the sample

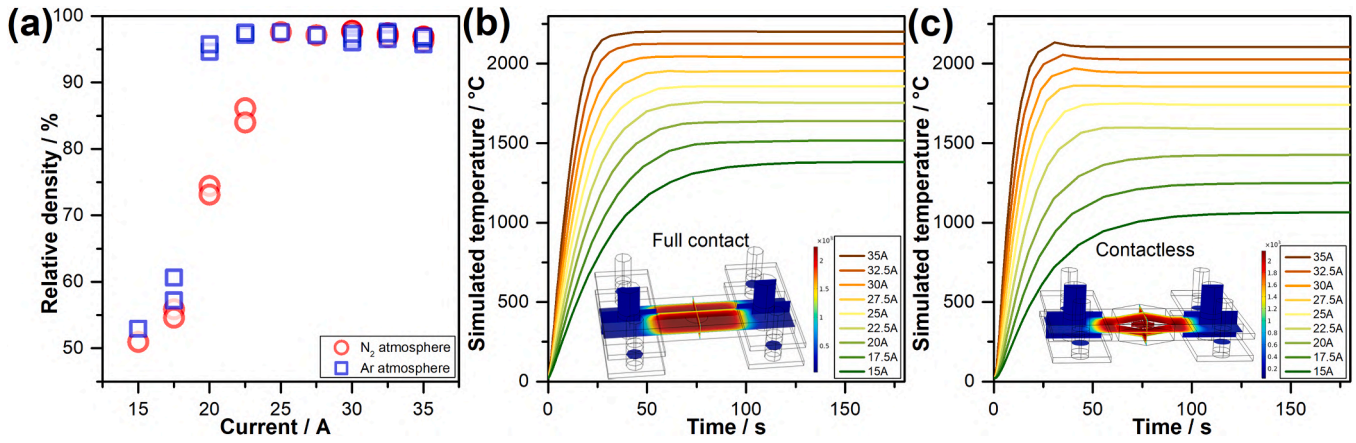

Fig. 1. (a) Relative density of 3YSZ samples treated under Ar and N_2 atmosphere as a function of current (each single point corresponds to a different sample); (b) Full contact, and (c) contactless simulation of the temperature range evolution upon UHS at different applied currents. The highest temperature is simulated by the Fem full-contact configuration and the lowest one by the contactless. Details about FEM are available in ref [30]. The relative density was calculated assuming the density of YSZ constant (6.05 g cm^{-3}).

reaches the equilibrium within about 1 min (Fig. 1**(b&c)**) the heating rates being well above 10^3 °C min^{-1}.

Well-densified bodies were obtained within 1 min UHS treatments both in Ar and N_2 but the current needed to achieve full densification is substantially different in the two cases, 20 A in Ar and 25 A in N_2. In general, the samples treated in N_2 require a higher current to sinter if compared with those treated in Ar.

The densification of the YSZ artifacts by UHS is confirmed by SEM micrographs taken on polished and thermally etched cross-sections (Fig. 2, taken at the sample center). Samples sintered under Ar at 20 and 22.5 A are already almost fully dense and show grain sizes of 0.24 ± 0.04 μm and 0.43 ± 0.15 μm, respectively. On the other hand, the samples treated under the same current under N_2 are still partially porous, in agreement with the density trend (Fig. 1**(a)**), and exhibit smaller grain size (0.11 ± 0.02 μm and 0.19 ± 0.06 μm under 20 and 22.5 A, respectively). It is worth noting that the sample produced in N_2

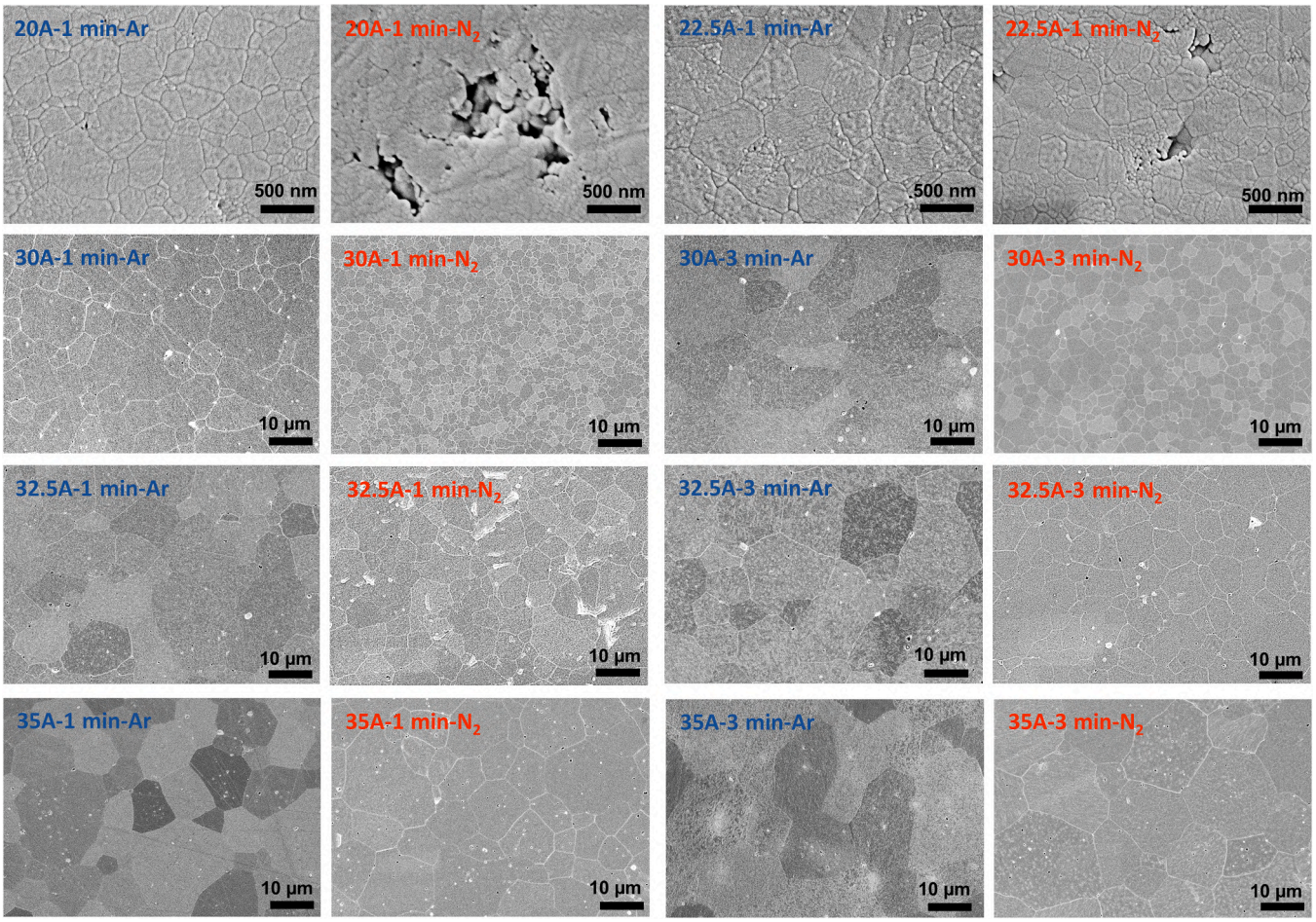

Fig. 2. SEM micrographs of polished cross-sections of the samples produced under different currents (A), dwell time (min), and environmental conditions (Ar or N_2).

at 22.5 A possesses a grain size similar to the sample fired in Ar under 20 A, although the Ar-treated sample is much denser (Fig. 1**(a)**). The result suggests that treatments in Ar are more efficient in promoting densification over coarsening. When UHS is carried out at higher currents (≥30 A), exaggerated grain growth occurs (note that the magnification increases 20 times in the different micrographs in Fig. 2). As expected, samples treated for 3 min are characterized by larger grains compared with those treated for 1 min (Table 1). Besides, the samples sintered under Ar generally possess larger grains than under N_2 for the same sintering conditions. Therefore, one can infer that the atmosphere (N_2 or Ar) impacts the microstructural evolution of YSZ during UHS.

We questioned whether these differences in densification and grain growth kinetics might originate from differences in the sample temperature under Ar and N_2 or form a reaction between nitrogen and YSZ, causing a substantial modification of the defect chemistry. To exclude the first hypothesis, we checked the current needed to melt a small piece of copper, platinum, and alumina within the UHS apparatus in Ar and N_2. No statistically reproducible difference between the two atmospheres was detected, thus pointing out that the same current results in the same felt temperature in Ar and N_2 (Fig S1). Also, the power dissipation in the two atmospheres is analogous under the same current density (Table S1). Hence, one can infer that thermal effects play a minor role and, consequently, some specific reactions between the oxide and the atmosphere must take place under N_2. Moreover, the melting point of the different compounds was compared with the simulated temperatures by FEM (Fig. S1), confirming that the FEM results are reliable and robust. Interestingly, the melting points of Pt and Al_2O_3 are very close to the upper temperature bound represented by the full contact configuration, this likely originating from the fact that at high temperatures most of the heat is quickly exchanged by radiation. On the other hand, the melting point of Cu lays more or less in the center of the simulated temperature interval reflecting the higher relevance at "low temperature" of the convective and conduction heat transfer.

XRD was used to point out possible reactions between zirconia and N_2 (Fig. 3). As expected, all the samples produced under Ar show clear diffraction features related to t-ZrO_2 (PDF-2 Card 96–210–0389), this result being also consistent with previous work on UHS of additively-manufactured 3YSZ structures [30]. On the other hand, the samples fired under N_2 remain tetragonal only at the lowest currents and then convert into c-ZrO_2 (PDF-2 Card 00–027–0997). This can be detected by the disappearance of the peaks doublet at around $2\theta \approx 35^\circ$ and 60° for currents > 30 A. In the most severe UHS conditions, we also observe the appearance of a rock salt-structured phase. The complete quantitative analysis is reported in Fig. 4**(a)**. The rock salt phase is consistent with ZrN (PDF-2 Card 00–035–0753), ZrO (PDF-2 Card 00–020–0684), or Zr(N,O) solid solution. These phases derive from an FCC Zr sublattice with the non-metals, either N and/or O, in the interstitial octahedral sites. It is not easy to differentiate between them by XRD since the lattice parameters are very similar to each other (0.4578 [57], 0.4577 [58], and 0.4580 nm [58] for ZrN, Zr(N,O), and ZrO, respectively). A certain uncertainness can also exist in the lattice parameter as a result of possible non-stoichiometry.

Furthermore, the Rietveld refinement of the patterns points out that tetragonality (Fig. 4**(b)**) of t-ZrO_2 progressively decreases from ≈1.014–1.015 to ≈1.09–1.10 as the current increases for UHS carried out in N_2 (note that the tetragonality was calculated only for samples where the amount of t-ZrO_2 was > 20 %, the refinement being not reliable for lower tetragonal phase load). Here, the tetragonality is defined as $c/a\sqrt{2}$, where c and a are the cell parameters of tetragonal zirconia. The ratio is equal to one for cubic crystals. In addition, the samples produced in Ar just show the diffraction features of t-YSZ (Fig. 4**(c)**). The tetragonality in Ar is quite stable though a slight decrease can be detected at increasing applied current.

Table 1
Grain size (in μm) after UHS under different currents/times in Ar and N_2.

Current / Time	Argon	Nitrogen
20 A / 1 min	0.24±0.04	0.11±0.02
22.5 A / 1 min	0.43±0.15	0.19±0.06
30 A / 1 min	5.4±2.9	1.4±0.1
30 A / 3 min	8.7±1.2	2.3±0.2
32.5 A / 1 min	8.5±0.7	4.8±1.4
32.5 A / 3 min	9.6±1.0	4.9±0.9
35 A / 1 min	8.6±0.8	8.1±1.3
35 A / 3 min	12.0±1.5	12.8±0.7

The phase evolution of the samples produced under N_2 was additionally investigated by Raman spectroscopy (Fig. 5). Raman is not very sensitive in differentiating between tetragonal and cubic zirconia but offers additional insight into the rock salt phase formation. The spectra for samples treated at low currents (17.5 A and 20 A) show the typical feature of *t*-ZrO_2, with the 321, 467 cm^{-1} (E_g modes) and strong 641 cm^{-1} peaks ($A_{1\,g}$) [59]. If the current exceeds 25–27.5 A in N_2, the spectra show clear features that can be ascribed to a rock salt phase, which becomes dominant under 30 A. These features include a shoulder at about 336 cm^{-1} (2TA), 390 cm^{-1} (TA+LA, weakly detected), the TO mode at about 460 cm^{-1} and the strong LO mode at 500 cm^{-1}. The broad feature at higher frequencies (560–659 cm^{-1}) is dominated by the TO-LA and LO+LA modes [60]. The Raman spectra are in general consistent with the XRD findings with one main difference: the formation of the rock salt is already detected at 27.5 A or even 25 A by Raman, whereas it can be identified only above 30 A by XRD, such a difference is not surprising since Raman being certainly more sensitive to the sample surface.

If the spectra of the rock salt are analyzed in more detail, one can observe that (i) the main peak (≈460 cm^{-1}) shifts at higher wavenumbers when increasing the treatment time and current, (ii) the Raman features become broader and less defined. The result seems consistent with the evolution of the rock salt phase from an O-rich to an N-rich one and in agreement with the spectra reported in the literature for YSZ flash sintered in Ar and N_2 [61].

The reaction between N_2 and YSZ is further confirmed by the sample coloration change during UHS (Fig. 6). In Ar, YSZ remains white up to 17.5 A, whereas at 20 A the oxide starts to darken, similarly to previous UHS results [31]. The blackening can originate from carbon contamination or oxide reduction which introduces donor levels a fraction of eV below the conduction band [62–64]. In the present work, no carbon contamination could originate from the binder burnout since the samples were pre-sintered before UHS. Contamination from the felt is possible, but this does not explain why the darkening onset in N_2 is delayed (between 22.5 A and 25 A). As a matter of fact, if the treating time or the current is increased, the darkening in Ar becomes more evident. On the other hand, the samples treated under N_2 at the highest currents turn goldish, acquiring a metallic aspect. Such gold-like coloration is a clear indication of ZrN or Zr(O,N) formation [58,65] as the ZrO rock salt appears as metallic dark grey [58].

XPS analyses were conducted on two samples sintered under the same conditions (30 A – 1 min) in Ar and N_2. The high-resolution N1s spectrum reveals a clear presence of nitrogen in the sample treated under N_2, such contribution missing in the Ar-processed sample (Fig. 7). Moreover, the position of this peak, with a maximum at 395.6 eV, is slightly lower than the expected 397.8 eV energy for a pure Zr-N bonding [66], very likely fitting with the expected value for oxynitride (ZrO)-N^{3-} in Zr(O, N) [66,67].

Zr3d spectrum was also collected on the same samples (Fig. 8). Clear low-energy Zr3d contributions (<181 eV) in the samples UHSed in N_2 are identified. The datasets were fitted using 2 (Ar) and 4 (N_2) Gaussian contributions. The two main peaks are located at 181.57(1) / 183.94(1) eV and 181.58(3) / 183.89(1) eV for Ar and N_2-sintered sample, respectively. These correspond to the $Zr3d_{5/2}$ and $Zr3d_{3/2}$ contributions and are very close to the literature values found for Y-doped ZrO_2 (181.6 and 184.0 eV) [68]. The energy separation between the two features is

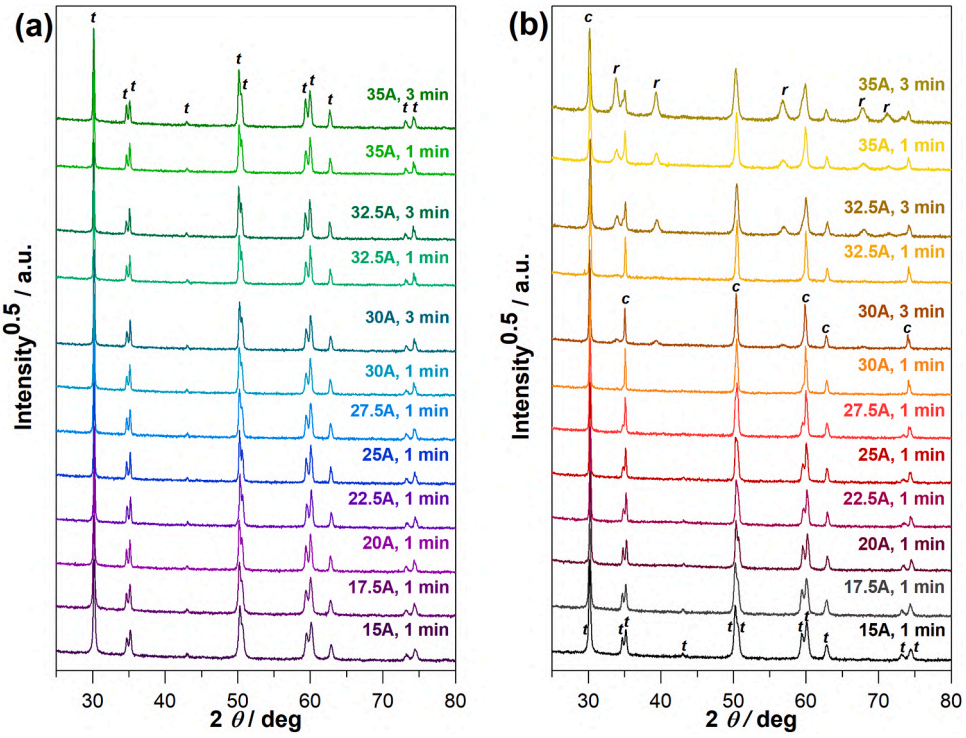

Fig. 3. XRD patterns for 3YSZ samples sintered at different currents and durations under (a) Ar and (b) N_2 atmosphere. The peaks are indexed as follows: t = tetragonal zirconia, c = cubic zirconia, r = rock salt.

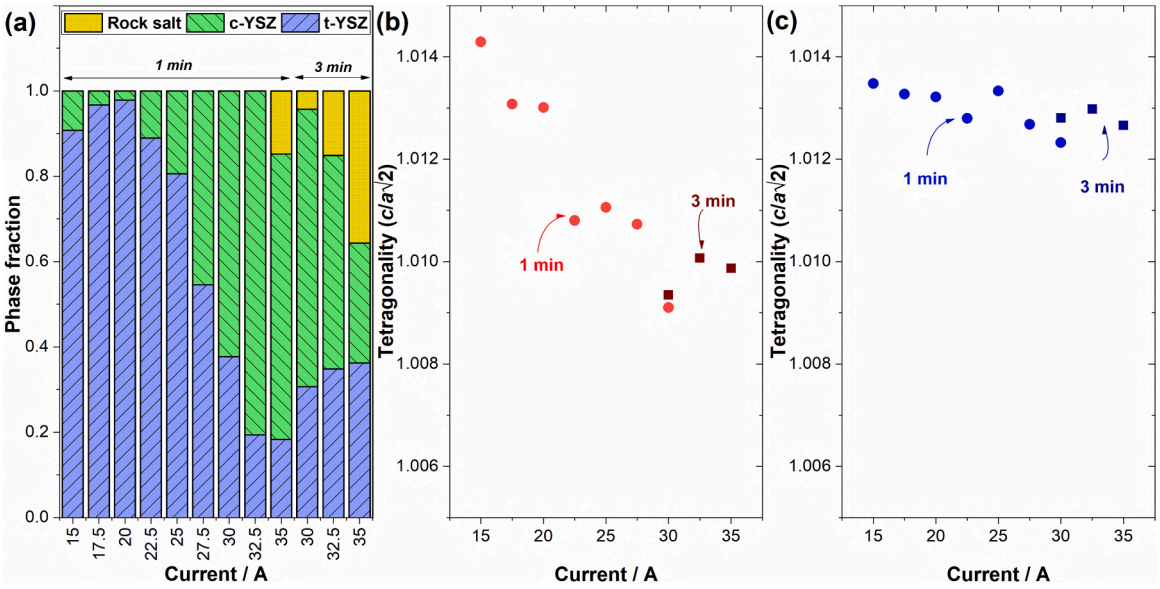

Fig. 4. (a) phase composition and (b) t-YSZ tetragonality evolution after UHS in N_2; (c) tetragonality for UHS in Ar atmosphere. Data obtained by Rietveld-refinement of the patterns in Fig. 3.

2.31 and 2.37 eV for the N_2 and Ar-processed samples respectively, which is close to the expected 2.4 eV [68]. The limited energy separation (2.31 eV) in N_2 is consistent with the formation of neighboring Zr-N bonding.

In the case of the N_2 sintered sample, however, additional contributions were fitted at 178.5(1) and 180.2(3) eV, which can be attributed to Zr-N binding energies [67,69]. These XPS data, both in the case of Zr3d and N1s spectra, confirm the reactivity between ZrO_2 and N_2 to form oxynitride compounds, as detected by Raman spectroscopy and XRD.

In order to check the possible carbon contamination in the specimen sintered at 30 A, C1s spectra were recorded on the surface of the sample and after 75 s etching. This (Fig. S2) shows a clear reduction of carbon content in the sample after a few seconds of etching, thus confirming that the contamination is restricted to the very top surface of the ceramic. Moreover, the presence of Zr-C bonding should be observed both in the Zr3d spectrum at 179.3 and 181.7 eV [70,71], which is not detected in Fig. 8 **a** and **b**, regardless the sintering atmosphere.

AC electrochemical impedance spectroscopy (EIS) was carried out from 200°C to 400°C in air. Fig. 9**(a,b)** shows the EIS Nyquist plots of

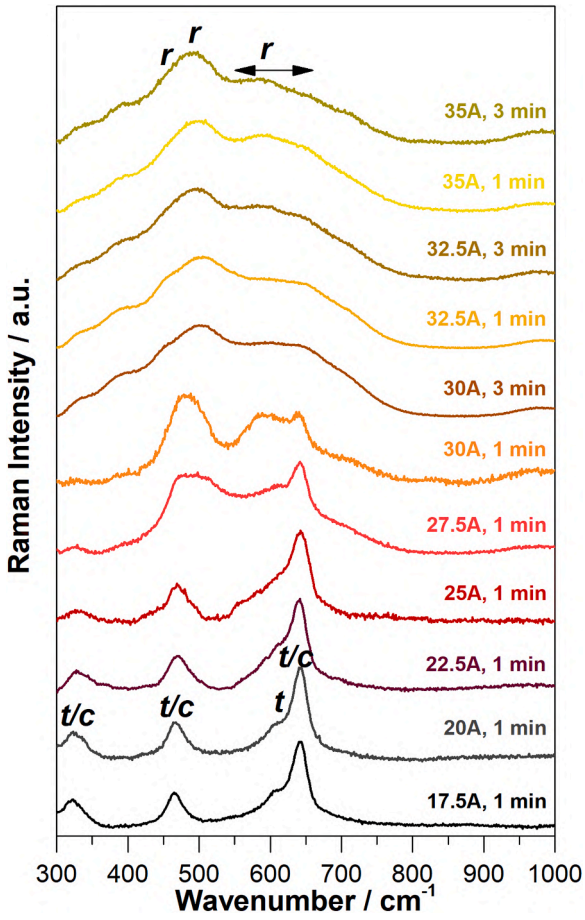

Fig. 5. Raman spectra of samples sintered under N_2 atmosphere. The peaks are indexed as follows: c = cubic, t = tetragonal YSZ, r = rock salt.

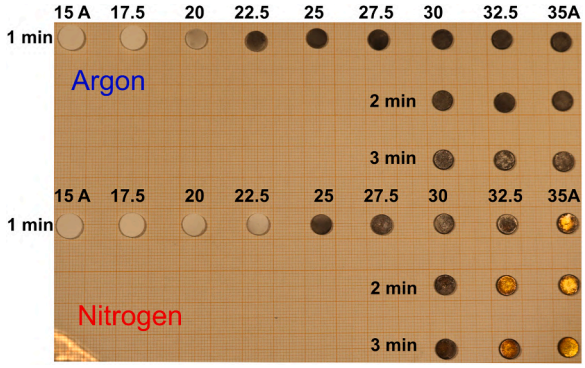

Fig. 6. Image of the samples under different current, time, and atmospheric (Ar and N_2) conditions.

impedance measured at 300°C for samples sintered in Ar and N_2 at various currents, along with the corresponding fits. For all samples, two contributions (semi-circles) are observed. The higher frequency one (left side) can be associated with bulk, while the lower frequency one (right side) corresponds to microstructural defects (grain boundaries, cracks, porosity, impurities) [72,73]. The right part of the plot at very low frequency corresponds to the electrode polarization in blocking conditions, thus confirming the ionic nature of the main charge carriers.

The bulk contribution is almost similar, with a resistivity of ≈ 0.15 MΩ.cm, for the three samples sintered in Ar (Fig. 9**(a)**) at 20, 22.5, and 30 A,. This suggests no major density evolution, as confirmed by the densification data in Fig. 1**(a)**. The low-frequency contribution shows a

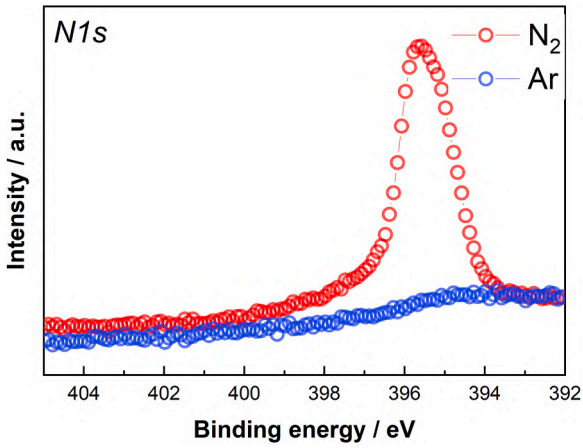

Fig. 7. XPS spectrum of N1s for samples sintered in Ar and N_2 at 30 A – 1 min.

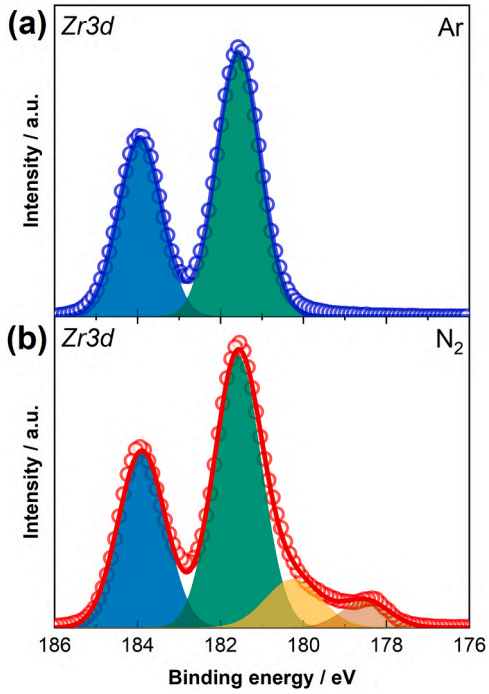

Fig. 8. XPS spectrum of Zr3d for samples sintered at 30 A for 1 min in (a) Ar and (b) N_2.

similar behavior from 20 to 22.5 A, then almost vanishes at 30 A. This confirms the elimination of microstructural defects, i.e. grain boundaries, in these sintering conditions (30 A in Ar). It is also consistent with the grain growth described previously (see Table 1) with an average grain size of 5.4 μm (30 A, Ar, 1 min).

Conversely, the samples sintered in N_2 (Fig. 9**(b)**) show a more important evolution of bulk contribution, with an impedance decrease visible between 20 A and 22.5 A. It can be explained by the density evolution of both samples, as demonstrated by Steil et al. [73]. According to the data obtained in 8 mol% doped YSZ, the density evolution fits with ~75 % of the bulk conductivity evolution. However, the incorporation of nitrogen ions influences the oxygen vacancy content, which may also contribute to the conductivity increase. A detailed description of the defects equilibria taking place in N_2 is reported in the Discussion section. Concerning the low-frequency contribution, the evolution between 20 A and 22.5 A is consistent with the density difference and the data becomes more complex at 30 A.

The impedance data from samples sintered at 30 A both in Ar and N_2

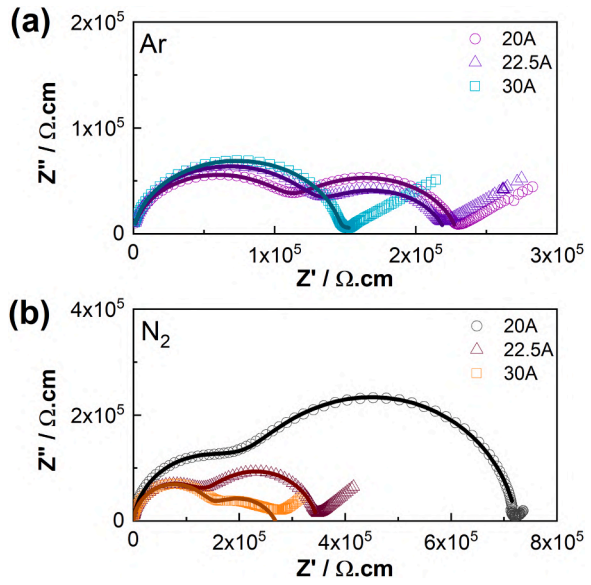

Fig. 9. Nyquist plot of complex impedance (300°C) of samples sintered under different currents in (a) Ar and (b) N_2. The fitting is represented by the solid lines.

are compared to the data obtained by M'Peko et al. [74] on 3YSZ powder sintered by Flash Sintering at 1A-900°C-60 s and presented in Fig. 10. As one can observe, the bulk contribution (left side) is of similar magnitude, thus confirming that the samples exhibit similar bulk ionic conductivity. However, the limited conductivity decrease observed in the samples can be related to the addition of partial electronic conduction in the material due to its partial reduction (see the blackening effect in Fig. 6). The main difference occurs at lower frequencies and it is related to the microstructure defects [72,73] in the samples. The flash-sintered sample exhibits higher resistivity, probably due to grain boundary (GB) blocking effects, while the samples sintered in UHS have lower resistivity. In the case of N_2 atmosphere, the sample faces partial phase change, which must explain the change in low-frequency contribution. This latter one cannot be fitted with a classical R-C or R-CPE contribution since the data are smeared over a wide range. The origin of such cannot be identified based on these measurements only but seems consistent with the formation of a secondary phase, namely Zr(O, N).

The impedance data (for the samples sintered under 10, 22.45, 30 A in Ar, and 20, 22.5 A in N_2) were fitted using two R-CPE contributions in series associated with bulk and GB parts. The results were used to calculate the conductivity, relaxation frequency, and capacitance (Fig. 11). Data for the sample sintered in N_2 at 30 A (see Fig. 10) could not be fitted in the low-frequency region, and only the data for the grain contribution are presented. Similarly, data for the sample sintered in Ar

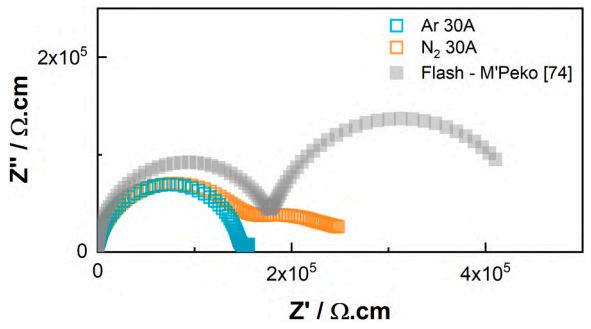

Fig. 10. Nyquist plot for impedance data of UHS sintered samples at 30 A in Ar and N_2 and data obtained by M'Peko et al. in Flash Sintering of 3YSZ at 900°C-1A-60 s [74].

at 30 A display a very low GB contribution compared to the bulk, therefore leading to a larger margin of error, which explains the variations observed especially in σ_{GB} and C_{GB}.

The GB conductivity drastically increased after sintering under 30 A in Ar (as highlighted in Fig. 9**(a)**). The activation energy for both bulk (b) and grain boundaries (GB) assumes similar values regardless of the UHS atmosphere, with the bulk between 0.84 and 0.88 eV and the GB in the range 0.96 – 1.00 eV. The only exception is the grain boundary contribution for the samples sintered under 30 A, which shows a slightly lower activation energy ≈ 0.9 eV. These values must be handled with care since they reflect an uncertainty related to its meager contribution to impedance. However, it has been shown before that the activation energy switches from ≈ 1 eV for ionic conductivity to 0.03 — 0.06 eV for electronic conductivity [75]. Therefore, the measured activation energies in this work confirm that the conduction is mainly driven by ionic conductivity, although a slight decrease (0.9 eV) for the sample sintered at 30 A might suggest a mixed conduction mechanism. Nevertheless, no sample is dominated by electronic conductivity. All relaxation frequencies are perfectly aligned both for bulk and GB contributions, confirming the similar nature of the relaxation phenomena. Finally, the bulk capacitances show temperature-independent values, similar for all samples (Fig. 11**(c,f)**). Conversely, one can notice the GB capacitance evolves with the UHS current. In particular, it increases with increasing applied current in both atmospheres. This can be associated with the evolution of microstructural defect nature and quantity [73]. GB capacitances for samples sintered in Ar are noticeably higher than in N_2. This suggests that these GB are affected by the atmosphere, probably by diffusion/reaction with N_2 preferentially in the GB even at the lowest currents (20 and 22.5 A).

Finally, we would like to remark that the EIS data points were collected by merging half data recorded while heating and half while cooling. The fact that the different contributions follow a regular trend points out that the sample evolution while EIS measurements are negligible from an electrochemical point of view. Besides, interpreting the Nyquist plots of complex impedance in N_2 atmosphere is challenging due to the complex phase and microstructural evolution occurring with increasing current (i.e., temperature). It should be clearly stated that future transmission electron microscopy (e.g., HRTEM and EELS) studies are necessary to understand the nitridation process including tetragonal-cubic phase transformation, and the nucleation and growth of the Zr(O, N) phase, in order to elucidate the various contributions to the observed low-frequency response. Consequently, further work is required to clarify these aspects.

4. Discussion

The temperature measurement upon UHS is a challenging issue as discussed previously, with strong experimental limitations when both thermocouples or pyrometers are used [76]. As such, calibrated FEM simulations represent a valuable approach for estimating the sample temperature. Since the main goal of this work was to observe the differences induced by UHS in N_2, the most important aspect is that the temperature achieved in Ar and N_2 is the same under the same applied current. This hypothesis was confirmed by some specific experiments where copper, platinum, and alumina were melted at the same current in the UHS setup under the two different atmospheres (Fig. S1). Furthermore, no statistically relevant differences in terms of power dissipation were identified when UHS was carried out in Ar and N_2 (Table S1).

The main outcome of this work is that the atmosphere plays a fundamental role when 3YSZ is processed by UHS. Substantial changes in terms of microstructural (Figs. 1 and 2) and phase evolution (Fig. 3) were detected.

Ruling out thermal effects as major sources for the different microstructure, one can infer that YSZ reacts with N_2 thus determining a substantial modification of the defect chemistry and self-diffusion

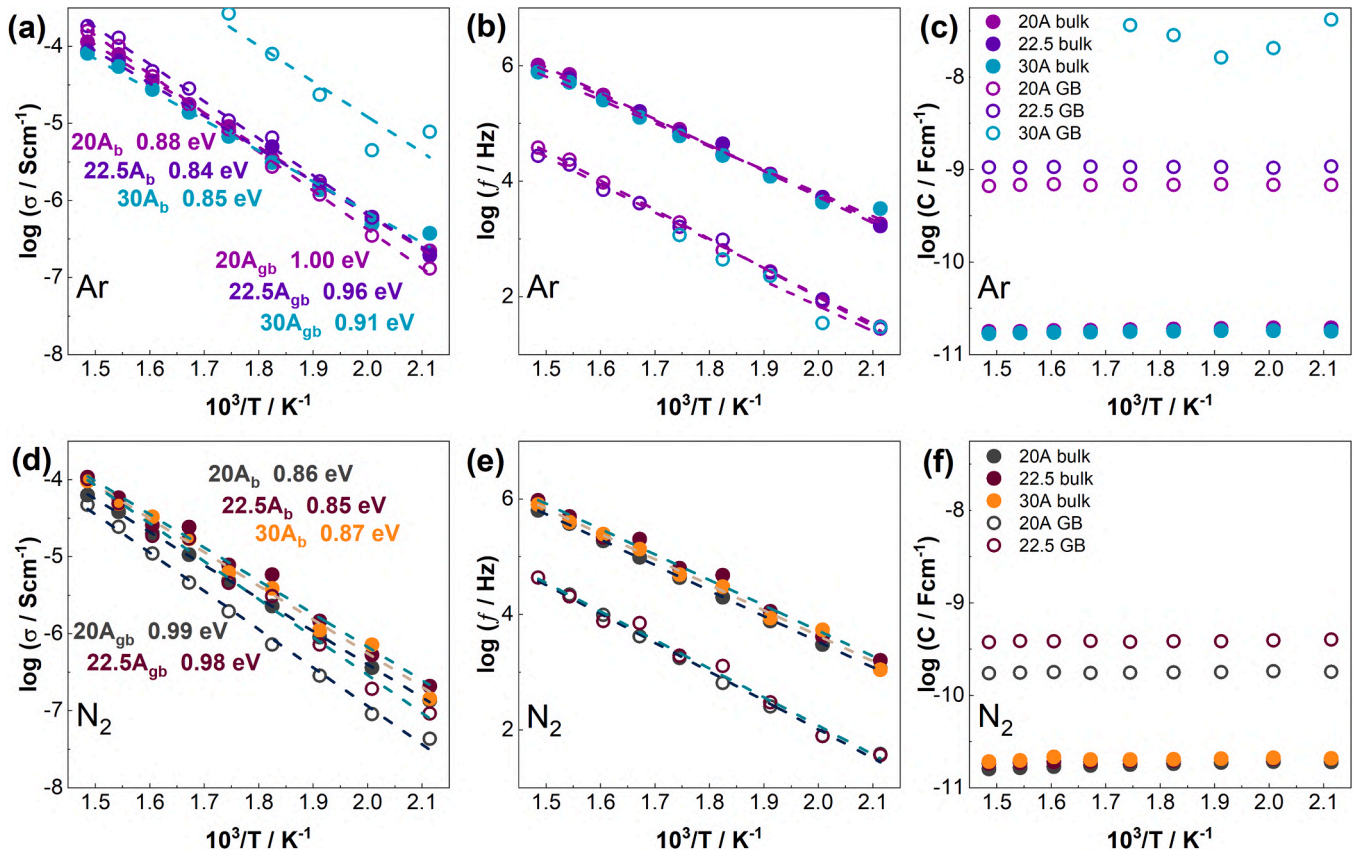

Fig. 11. Data obtained from EIS measurements fits for samples produced in (a-c) Ar and (d-f) N_2 (a, d) conductivity, (b, e) relaxation frequency (c, f) equivalent capacitance.

kinetics. The reaction between YSZ and nitrogen is further confirmed by the fact that after UHS one can observe that (i) t-ZrO_2 decreases its tetragonality, (ii) c-ZrO_2 forms, (iii) a rock salt oxynitride is produced and (iv) the grain boundary capacitance varies. The formation of the rock salt phase is confirmed by Raman spectroscopy (Fig. 5) and XRD (Fig. 3), its oxynitride nature being detected by XPS (Figs. 7 and 8) and corroborated by the chromatic alteration (Fig. 6) of the samples after UHS. The results resemble those obtained by Morisaki et al. [65] and, more recently, by Bechteler and Todd [58] in YSZ produced by flash sintering in N_2. In those cases, the sample reduction was forced by an electric current application; herein, by the high temperature combined with a highly reducing environment (presence of graphitic carbon).

Said structural features are typically accounted for by oxygen vacancy formation, which tends to stabilize the fluorite structure and reduce the tetragonal distortion of the lattice [77,78]. In fact, the formation of O vacancy in most cases is a result of doping with trivalent cations:

$$M_2O_3 \xrightarrow{ZrO_2} 2M'_{Zr} + V_O^{\bullet\bullet} + 3O_o^x \quad (1)$$

although, it could also originate from the doping of the anionic site with trivalent cations, like nitrogen:

$$2N_2 + 6O_O^x \xrightarrow{ZrO_2} 4N'_O + 2V_O^{\bullet\bullet} + 3O_2 \quad (2)$$

Therefore, N^{3-} anionic site doping has an effect analogous to Y^{3+} cationic site doping. If one looks at the literature, 3YSZ sintered under conventional conditions possess a tetragonality of about 1.014, such value agrees with our measurements on the samples UHSed at the lowest currents in N_2 (Fig. 4). However, higher UHS currents in N_2 lead to a substantial drop in tetragonality, it can be as low as 1.009 in N_2 (≈30 A), which corresponds to Y-doping between 4 and 5 mol% [77]. The "additional doping" effect must originate from the reaction with the atmosphere, i.e. the incorporation of N in the lattice. If the current and the UHS time increase further, a heavy reduction occurs, leading to the formation of the rock salt phase in N_2. On the other hand, the tetragonality in Ar is quite stable; nevertheless, a slight decrease can be identified when the current increases. Reducing conditions (which create oxygen vacancies) are known to shift the system to lower tetragonality phases [79]. The impact of UHS in Ar on tetragonality is definitively smaller than in N_2, suggesting a lower concentration of oxygen vacancies as discussed below.

Two reactions —reduction and nitridation— are required to convert tetragonal zirconia into cubic zirconia and then oxynitride. The first one takes place also in Ar and can be written as:

$$C + O_o^x \xrightarrow{ZrO_2} CO + V_O^{\bullet\bullet} + 2e' \quad (3)$$

where C can come from the felt. Native reduction is also possible though less likely:

$$2O_O^x \xrightarrow{ZrO_2} O_2 + 2V_O^{\bullet\bullet} + 4e' \quad (4)$$

As such, UHS under both Ar and N_2 causes the formation of oxygen vacancies and free electrons. One must note that both reactions move to the right at high temperatures due to the evolution of a gas phase. However, due to the high and negative formation energy of ZrO_2, the reactions cannot proceed to the right "forever". It is important to remember that zirconia lies below CO in the Ellingham diagram even at 2300°C; therefore, in standard conditions, its total reduction to metallic zirconium is not possible [80].

On the other hand, the electrons created by Eqs.3 and 4 can react with N_2, reducing it into nitrogen ions, which can be incorporated into the YSZ lattice (as previously reported in the literature [65,81]):

$$3V_O^{\bullet\bullet} + 6e' + N_2 \xrightarrow{ZrO_2} V_O^{\bullet\bullet} + 2N'_o \quad (5)$$

Such a reaction removes the electrons (and, partially, the oxygen vacancies), which are the product of Eqs. 3 and 4; therefore, it allows them to prosecute and move further to the right. The overall reaction in nitrogen can be written as:

$$3C + N_2 + 3O_o^x \xrightarrow{ZrO_2} 3CO + V_O^{\bullet\bullet} + 2N' \quad (6)$$

or

$$2N_2 + 6O_o^x \xrightarrow{ZrO_2} 2\,V_O^{\bullet\bullet} + 4N'_o + 3O_2 \quad (7)$$

As O_2 is indeed more oxidant than N_2 we expect that Eq. 6, where the oxygen release is mediated by the formation of CO, is dominant. In summary, one can infer that the presence of N_2 in the UHS atmosphere (i) allows the formation of a higher amount of oxygen vacancies compared to Ar as they are stabilized by the net negative charge on the nitrogen dopants, and (ii) the conditions are "less reducing" considering that the free electrons from Eqs. 3 and 4 are partially consumed by Eq. 5 and are not available to reduce the average oxidation state of cations. This is testified by the fact that the overall reactions (Eqs. 6 and 7) do not contain any free electrons on the right side and do not involve any change in the oxidation state of the cations.

The abovementioned reactions perfectly match the experimental results: the formation of extra oxygen vacancy through the reaction in Eqs. 6 and 7 are in agreement with a reduction of the cell tetragonality and with the stabilization of the fluorite cubic structure. Indeed, when reactions in Eqs. 6 and 7 move to the right, approaching the solubility limit of N in YSZ, rock salt oxynitride precipitates [44].

Considering the formation of the rock salt phase we can infer that it could form through different reactions which are listed below (assuming for convenience that its final composition is ZrN for which we found thermochemical data):

$$2ZrO_2 + N_{2(g)} \rightarrow 2ZrN + 2O_{2(g)} \quad (8)$$

$$2ZrO_2 + 4C + N_{2(g)} \rightarrow 2ZrN + 4CO_{(g)} \quad (9)$$

$$2ZrO_2 + 2C + N_{2(g)} \rightarrow 2ZrN + 2CO_{2(g)} \quad (10)$$

$$2ZrO_2 + 4CO_{(g)} + N_{2(g)} \rightarrow 2ZrN + 4CO_{2(g)} \quad (11)$$

The first reaction assumes a native reduction of zirconia with spontaneous release of molecular oxygen at high temperatures. Eqs. 9 and 10 assume that the reduction of zirconia is promoted by the presence of graphitic C, releasing carbon monoxide or dioxide. In Eq. 11, the reducing agent is CO. Using the thermochemical data available in [82] we can calculate the standard free energy change associated with the different reactions, the results are reported in Fig. 12**(a)**. We can observe that in standard conditions the only reaction moving to the right at high temperature, with the formation of ZrN, is the one where zirconia is reduced by carbon releasing CO (Eq. 9). In particular, ΔG^0 becomes negative for temperatures exceeding $\approx$ 1600°C. Moreover, we can calculate the partial pressure of the different gasses at the thermodynamic equilibrium for the reactions in Eqs. 8, 9, 10, and 11 as follows:

$$(pO_2)^2 = k_{eq.Eq8} = \exp(-\Delta G^0_{Eq8} / RT) \quad (12)$$

$$(pCO)^4 = k_{eq.Eq9} = \exp(-\Delta G^0_{Eq9} / RT) \quad (13)$$

$$(pCO_2)^2 = k_{eq.Eq10} = \exp(-\Delta G^0_{Eq10} / RT) \quad (14)$$

$$(pCO_2/pCO)^4 = k_{eq.Eq11} = \exp(-\Delta G^0_{Eq11} / RT) \quad (15)$$

The equilibria in the previous equations were written under the following assumptions: (i) the chemical activity of the solids is assumed equal to one; (ii) the activity of N_2 is close to one (partial pressure of N_2 is close to ambient pressure); (iii) the activity of the gases can be approximated with their partial pressure. The results reported in Fig. 12 **(b)** confirm that: (i) it is thermodynamically impossible to form ZrN through the spontaneous reduction of ZrO_2 (Eq. 8); (ii) the reaction including CO_2 as a product is extremely unlikely with the partial pressure of CO_2 at the equilibrium < 0.01 atm even at temperature approaching the melting point of zirconia; (iii) the reaction in Eq. 9 is possible and spontaneous. On these bases, we can infer that the formation of the rock salt phase is mainly mediated by the formation of CO as a result of the reaction between carbon and the oxide.

The defect reactions also explain why blackening is observed at higher currents in N_2 if compared with Ar (Fig. 7). YSZ darkening is associated with the visible light absorption by free electrons, Zr^{3+} (Zr'_{Zr}), F (V_O^x) and F^+ ($V_O^\bullet$) centers which form through the following reactions:

$$Zr_{Zr}^x + e' \longrightarrow Zr'_{Zr} \quad (16)$$

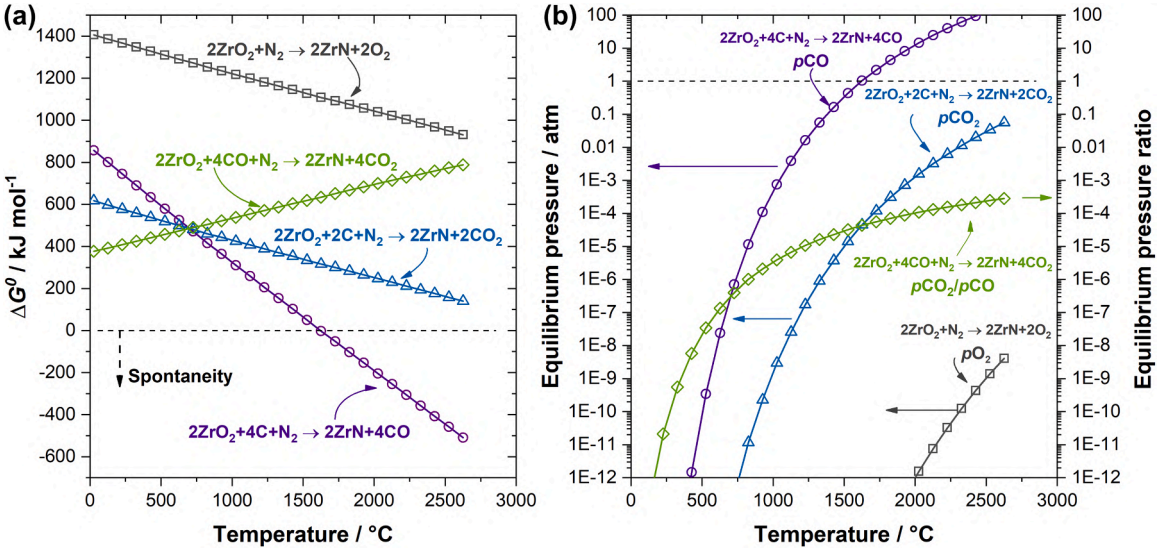

Fig. 12. a) Standard Gibbs free energy change associated to different possible reaction leading to the formation of ZrN in UHS; b) partial pressure of the different gasses at the equilibrium calculated using Eqs. 12–15. Thermochemical data taken from [82].

$$V_O^{\bullet\bullet} + 2e' \longrightarrow V_O^{\bullet} + e' \longrightarrow V_O^{x} \quad (17)$$

Zr'_{Zr} is a donor state located only 0.2 eV below the conduction band edge. F and F^+ centers represent deeper levels, about 2 eV below the conduction band [64], but can still absorb most of the visible light (≈1.7–2.7 eV). Indeed, the free electron consumption by nitrogen reduction (Eq. 5) hinders reactions in Eqs. 16 and 17 by reducing the concentration of one of the reagents. On the other hand, Eq. 5 causes the formation of N'_o which is an acceptor level laying 2.8 eV above the valence band edge [83] thus being optically inactive in the visible spectrum.

The effect of the atmosphere on the phase evolution appears therefore consistent and robust. It is less straightforward the reason why we observe a substantial change in the densification and grain growth kinetics in different atmospheres (Figs. 1 and 2). Although the conclusion is not definitive, one can point out that there is already solid literature evidencing the beneficial effect of reducing conditions on mass transport, especially referred to as grain growth, in fluorite-structured oxides [84–88]. For instance, Dong [88] reported a decrease in the energy barrier for Zr diffusion in YSZ along the [1 1 0] direction from 4.31 to 3.17 eV for the unreduced Zr^{4+} and reduced Zr^{3+} cations, respectively. In a recent paper, Martin et al. [89] have also shown the beneficial effect of reducing conditions on the sintering of YSZ. In the UHS experiments carried out in the present work, the treatments in Ar are more reducing than those in N_2: the free electrons are consumed to reduce nitrogen and, therefore, are not available for the reaction in Eq. 16, which allows the formation of Zr^{3+}. Hence, one can infer as a possible explanation that the reduction-induced boosting effect on densification observed in Ar cannot be reproduced to the same extent in nitrogen.

Along with these observations, impedance data show that the bulk ionic conductivity is not affected by the atmosphere, and the measured values are substantially consistent with what is expected from the literature for both conventional and flash-sintered samples [74]. Nevertheless, the grain boundaries show an important modification of their impedance behavior. In particular, N_2 atmosphere modifies the phase compositions, which in turn influences the impedance data of GB contributions. This is particularly visible at 30 A, with a low-frequency response containing various different contributions (Fig. 10). However, differences can be spotted also in terms of grain boundary capacitance values which are reduced in N_2 even under modest UHS currents. This suggests once again that N_2 interacts with the material even at relatively low UHS currents. Despite the result could seem in partial contradiction with XRD data (not showing a substantial formation of c-ZrO_2 at such currents), one should bear in mind that EIS provides resistivity information and, therefore, it is highly sensitive to phases present in the grain boundaries or on the local GB defect chemistry (the difference between GB specific conductivity and bulk conductivity is around 1.5 order of magnitude). Consequently, it is much more sensitive to what happens at the interfaces, including chemical or structural changes, although their volume or quantity is not sufficient to be detected by XRD or Raman spectroscopy.

The differences in GB capacitance between UHS in N_2 and Ar point out that the properties of UHS sintered samples (or flash sintered) do not originate from the rapid heating/cooling only, but must probably account also for additional effects. We could speculate that the heavily reducing conditions generated by flash and UHS in Ar (already discussed that UHS in N_2 is “less reducing”) play a role. The samples UHSed under 30 A show, in any case, a remarkable effect: an increase of ionic conductivity, particularly in Ar, leading to negligible blocking effect at the grain boundaries. UHS therefore enables the production of an ionic conductor whose conductivity is driven by the bulk properties only.

5. Conclusions

The UHS atmosphere impacts both the microstructural and phase evolution of 3YSZ. In N_2, highly densified samples can be obtained at 25 A, whereas in the Ar atmosphere densification is anticipated at around 20 A. A similar trend is shown also in terms of grain growth. While the samples treated under Ar always remain tetragonal, those treated in N_2 exhibit at first a reduction of the cell tetragonality and then the stabilization of cubic zirconia, and eventually the formation of a rock salt oxynitride.

The results can be explained by assuming the incorporation of nitrogen in the ZrO_2 lattice which was further confirmed by XPS. The anionic solid solution results in the formation of oxygen vacancies for charge compensation which stabilize cubic zirconia and reduce the tetragonality of t-ZrO_2. Furthermore, molecular N_2 reduction to N^{3-} ions incorporated in the lattice can also explain the different chromatic alteration of the specimen and, at least partially, the delayed densification under N_2.

In addition to the phase and microstructural evolution, UHS in dissimilar atmospheres leads to different electrochemical properties of YSZ at the grain boundaries. Remarkably high values of ionic conductivity were obtained after UHS under 30 A with substantially negligible blocking effect from the grain boundaries.

CRediT authorship contribution statement

Levent Karacasulu: Writing – original draft, Visualization, Methodology, Investigation, Conceptualization. **Thomas de Beauvoir:** Writing – original draft, Methodology, Investigation, Data curation, Conceptualization. **Emanuele De Bona:** Investigation, Data curation. **Michele Cassetta:** Investigation, Data curation. **Cekdar Vakifahmetoglu:** Writing – review & editing, Supervision. **Vincenzo Sglavo:** Writing – review & editing, Supervision, Resources. **Mauro Bortolotti:** Investigation, Data curation. **Charles Maniére:** Visualization, Software, Data curation. **Claude Estournés:** Writing – review & editing, Supervision, Resources. **Mattia Biesuz:** Writing – review & editing, Supervision, Methodology, Conceptualization.

Declaration of Competing Interest

The authors declare that they have no known competing financial interests or personal relationships that could have appeared to influence the work reported in this paper.

Acknowledgments

Levent Karacasulu acknowledges the support of TUBITAK (The Scientific and Technological Research Council of Türkiye) within 2214-A - International Research Fellowship Programme for PhD students. VMS acknowledges the European Union under NextGenerationEU, PRIN 2022 Prot. N. 2022KWSRSA.

Appendix A. Supporting information

Supplementary data associated with this article can be found in the online version at doi:10.1016/j.jeurceramsoc.2024.116879.

References

[1] R.K. Bordia, S.-J.L. Kang, E.A. Olevsky, Current understanding and future research directions at the onset of the next century of sintering science and technology, J. Am. Ceram. Soc. 100 (2017) 2314–2352, https://doi.org/10.1111/jace.14919.
[2] S. Grasso, Y. Sakka, G. Maizza, Electric current activated/assisted sintering (ECAS): a review of patents 1906–2008, Sci. Technol. Adv. Mater. 10 (2009) 053001, https://doi.org/10.1088/1468-6996/10/5/053001.
[3] O. Guillon, J. Gonzalez-Julian, B. Dargatz, T. Kessel, G. Schierning, J. Räthel, M. Herrmann, Field-Assisted Sintering Technology/Spark Plasma Sintering: Mechanisms, Materials, and Technology Developments, Adv. Eng. Mater. 16 (2014) 830–849, https://doi.org/10.1002/adem.201300409.
[4] M. Biesuz, S. Grasso, V.M. Sglavo, What’s new in ceramics sintering? A short report on the latest trends and future prospects, Curr. Opin. Solid State Mater. Sci. 24 (2020) 100868, https://doi.org/10.1016/j.cossms.2020.100868.

[5] M. Bram, A.M. Laptev, T.P. Mishra, K. Nur, M. Kindelmann, M. Ihrig, J.G. Pereira da Silva, R. Steinert, H.P. Buchkremer, A. Litnovsky, F. Klein, J. Gonzalez-Julian, O. Guillon, Application of Electric Current-Assisted Sintering Techniques for the Processing of Advanced Materials, Adv. Eng. Mater. 22 (2020) 2000051, https://doi.org/10.1002/adem.202000051.

[6] C. Vakifahmetoglu, L. Karacasulu, Cold sintering of ceramics and glasses: A review, Curr. Opin. Solid State Mater. Sci. 24 (2020) 100807, https://doi.org/10.1016/j.cossms.2020.100807.

[7] R. Orrù, R. Licheri, A.M. Locci, A. Cincotti, G. Cao, Consolidation/synthesis of materials by electric current activated/assisted sintering, Mater. Sci. Eng.: R: Rep. 63 (2009) 127–287, https://doi.org/10.1016/j.mser.2008.09.003.

[8] O. Guillon, C. Elsässer, O. Gutfleisch, J. Janek, S. Korte-Kerzel, D. Raabe, C. A. Volkert, Manipulation of matter by electric and magnetic fields: Toward novel synthesis and processing routes of inorganic materials, Mater. Today 21 (2018) 527–536, https://doi.org/10.1016/j.mattod.2018.03.026.

[9] M. Biesuz, T. Saunders, D. Ke, M.J. Reece, C. Hu, S. Grasso, A review of electromagnetic processing of materials (EPM): Heating, sintering, joining and forming, J. Mater. Sci. Technol. 69 (2021) 239–272, https://doi.org/10.1016/j.jmst.2020.06.049.

[10] J. Guo, R. Floyd, S. Lowum, J.-P. Maria, T. Herisson de Beauvoir, J.-H. Seo, C. A. Randall, Cold Sintering: Progress, Challenges, and Future Opportunities, Annu. Rev. Mater. Res 49 (2019) 275–295, https://doi.org/10.1146/annurev-matsci-070218-010041.

[11] Z.A. Munir, U. Anselmi-Tamburini, M. Ohyanagi, The effect of electric field and pressure on the synthesis and consolidation of materials: A review of the spark plasma sintering method, J. Mater. Sci. 41 (2006) 763–777, https://doi.org/10.1007/s10853-006-6555-2.

[12] D. Agrawal, 9 - Microwave sintering of ceramics, composites and metal powders, in: Z.Z. Fang (Ed.), Sintering of Advanced Materials, Woodhead Publishing, 2010, pp. 222–248, https://doi.org/10.1533/9781845699949.2.222.

[13] M.N. Rahaman, Ceramic processing and sintering, CRC press, 2017.

[14] L. Porz, M. Scherer, D. Huhn, L.-M. Heine, S. Britten, L. Rebohle, M. Neubert, M. Brown, P. Lascelles, R. Kitson, D. Rettenwander, L. Fulanovic, E. Bruder, P. Breckner, D. Isaia, T. Frömling, J. Rödel, W. Rheinheimer, Blacklight sintering of ceramics, Mater. Horiz. 9 (2022) 1717–1726, https://doi.org/10.1039/D2MH00177B.

[15] C. Wang, W. Ping, Q. Bai, H. Cui, R. Hensleigh, R. Wang, A.H. Brozena, Z. Xu, J. Dai, Y. Pei, A general method to synthesize and sinter bulk ceramics in seconds, Science 368 (1979) (2020) 521–526, https://doi.org/10.1126/science.aaz7681.

[16] M. Biesuz, V.M. Sglavo, Flash sintering of ceramics, J. Eur. Ceram. Soc. 39 (2019) 115–143, https://doi.org/10.1016/j.jeurceramsoc.2018.08.048.

[17] M. Yu, S. Grasso, R. Mckinnon, T. Saunders, M.J. Reece, Review of flash sintering: materials, mechanisms and modelling, Adv. Appl. Ceram. 116 (2017) 24–60, https://doi.org/10.1080/17436753.2016.1251051.

[18] M. Ihrig, T.P. Mishra, W.S. Scheld, G. Häuschen, W. Rheinheimer, M. Bram, M. Finsterbusch, O. Guillon, $Li_7La_3Zr_2O_{12}$ solid electrolyte sintered by the ultrafast high-temperature method, J. Eur. Ceram. Soc. 41 (2021) 6075–6079, https://doi.org/10.1016/j.jeurceramsoc.2021.05.041.

[19] T.P. Mishra, S. Wang, C. Lenser, D. Jennings, M. Kindelmann, W. Rheinheimer, C. Broeckmann, M. Bram, O. Guillon, Ultra-fast high-temperature sintering of strontium titanate, Acta Mater 231 (2022) 117918, https://doi.org/10.1016/j.actamat.2022.117918.

[20] M. Biesuz, A. Galotta, A. Motta, M. Kermani, S. Grasso, J. Vontorová, V. Tyrpekl, M. Vilémová, V.M. Sglavo, Speedy bioceramics: Rapid densification of tricalcium phosphate by ultrafast high-temperature sintering, Mater. Sci. Eng.: C. 127 (2021) 112246, https://doi.org/10.1016/j.msec.2021.112246.

[21] J. Dong, V. Pouchly, M. Biesuz, V. Tyrpekl, M. Vilémová, M. Kermani, M. Reece, C. Hu, S. Grasso, Thermally-insulated ultra-fast high temperature sintering (UHS) of zirconia: A master sintering curve analysis, Scr. Mater. 203 (2021) 114076, https://doi.org/10.1016/j.scriptamat.2021.114076.

[22] R.-X. Luo, M. Kermani, Z.-L. Guo, J. Dong, C.-F. Hu, F. Zuo, S. Grasso, B.-B. Jiang, G.-L. Nie, Z.-Q. Yan, Ultrafast high-temperature sintering of silicon nitride: A comparison with the state-of-the-art techniques, J. Eur. Ceram. Soc. 41 (2021) 6338–6345, https://doi.org/10.1016/j.jeurceramsoc.2021.06.021.

[23] M. Kermani, J. Dong, M. Biesuz, Y. Linx, H. Deng, V.M. Sglavo, M.J. Reece, C. Hu, S. Grasso, Ultrafast high-temperature sintering (UHS) of fine grained α-Al_2O_3, J. Eur. Ceram. Soc. 41 (2021) 6626–6633, https://doi.org/10.1016/j.jeurceramsoc.2021.05.056.

[24] R.-F. Guo, H.-R. Mao, Z.-T. Zhao, P. Shen, Ultrafast high-temperature sintering of bulk oxides, Scr. Mater. 193 (2021) 103–107, https://doi.org/10.1016/j.scriptamat.2020.10.045.

[25] A. Alemayehu, M. Biesuz, K.Y. Javan, A. Tkach, P.M. Vilarinho, V.M. Sglavo, V. Tyrpekl, Ultrafast high-temperature sintering of gadolinia-doped ceria, J. Eur. Ceram. Soc. 43 (2023) 4837–4843, https://doi.org/10.1016/j.jeurceramsoc.2023.04.025.

[26] S. Wang, T.P. Mishra, Y. Deng, L. Balice, A. Kaletsch, M. Bram, C. Broeckmann, Electric Current-Assisted Sintering of 8YSZ: A Comparative Study of Ultrafast High-Temperature Sintering and Flash Sintering, Adv. Eng. Mater. 25 (2023) 2300145, https://doi.org/10.1002/adem.202300145.

[27] Y. Zhao, H. Li, Y. Zu, Y. Wang, X. Fu, W. Zhou, G. Chen, (MgCoNiCuZn)O with particular microstructure and distinctive electrochemical performance prepared using ultrafast high-temperature sintering, J. Eur. Ceram. Soc. 43 (2023) 7573–7580, https://doi.org/10.1016/j.jeurceramsoc.2023.07.062.

[28] R.-F. Guo, H.-R. Mao, P. Shen, Ultra-fast high-temperature synthesis and densification of high-entropy diborides and diboride-carbide ceramics, J. Eur. Ceram. Soc. 43 (2023) 5763–5773, https://doi.org/10.1016/j.jeurceramsoc.2023.05.042.

[29] E. De Bona, C. Manière, V.M. Sglavo, M. Biesuz, Ultrafast high-temperature sintering (UHS) of ZrB_2-based materials, J. Eur. Ceram. Soc. 44 (2024) 567–573, https://doi.org/10.1016/j.jeurceramsoc.2023.09.007.

[30] S. Bhandari, C. Manière, F. Sedona, E. De Bona, V.M. Sglavo, P. Colombo, L. Fambri, M. Biesuz, G. Franchin, Ultra-rapid debinding and sintering of additively manufactured ceramics by ultrafast high-temperature sintering, J. Eur. Ceram. Soc. 44 (2024) 328–340, https://doi.org/10.1016/j.jeurceramsoc.2023.08.040.

[31] T. Che, H.-R. Mao, R.-F. Guo, P. Shen, Ultrafast synthesis and pressureless densification of multicomponent nitride and carbonitride ceramics, Ceram. Int 49 (2023) 31530–31538, https://doi.org/10.1016/j.ceramint.2023.07.104.

[32] Z.-T. Zhao, R.-F. Guo, H.-R. Mao, P. Shen, Effect of components on the microstructures and properties of rare-earth zirconate ceramics prepared by ultrafast high-throughput sintering, J. Eur. Ceram. Soc. 41 (2021) 5768–5773, https://doi.org/10.1016/j.jeurceramsoc.2021.04.053.

[33] H.-R. Mao, E.-T. Dong, S.-B. Jin, X.-M. Qiu, P. Shen, Ultrafast high-temperature synthesis and densification of high-entropy carbides, J. Eur. Ceram. Soc. 42 (2022) 4053–4065, https://doi.org/10.1016/j.jeurceramsoc.2022.03.054.

[34] R. Wang, W. Ping, C. Wang, Y. Liu, J. Gao, Q. Dong, X. Wang, Y. Mo, L. Hu, Computation-Guided Synthesis of New Garnet-Type Solid-State Electrolytes via an Ultrafast Sintering Technique, Adv. Mater. 32 (2020) 2005059, https://doi.org/10.1002/adma.202005059.

[35] J. Wu, M. kermani, D. Zhu, J. Li, Y. Lin, C. Hu, S. Grasso, Carbon free ultra-fast high temperature sintering of translucent zirconia, Scr. Mater. 210 (2022) 114476, https://doi.org/10.1016/j.scriptamat.2021.114476.

[36] Y. Lin, N. Luo, E. Quattrocchi, F. Ciucci, J. Wu, M. Kermani, J. Dong, C. Hu, S. Grasso, Ultrafast high-temperature sintering (UHS) of $Li_{1.3}Al_{0.3}Ti_{1.7}(PO_4)_3$, Ceram. Int 47 (2021) 21982–21987, https://doi.org/10.1016/j.ceramint.2021.04.216.

[37] A. Flaureau, A. Weibel, G. Chevallier, C. Estournès, Study of the densification and grain growth mechanisms occurring during spark plasma sintering of different submicronic yttria-stabilized zirconia powders, J. Eur. Ceram. Soc. 41 (2021) 3581–3594, https://doi.org/10.1016/j.jeurceramsoc.2021.01.032.

[38] P. Aldebert, J.-P. Traverse, Structure and Ionic Mobility of Zirconia at High Temperature, J. Am. Ceram. Soc. 68 (1985) 34–40, https://doi.org/10.1111/j.1151-2916.1985.tb15247.x.

[39] T.-J. Chung, H. Song, G.-H. Kim, D.-Y. Kim, Microstructure and Phase Stability of Yttria-Doped Tetragonal Zirconia Polycrystals Heat Treated in Nitrogen Atmosphere, J. Am. Ceram. Soc. 80 (1997) 2607–2612, https://doi.org/10.1111/j.1151-2916.1997.tb03163.x.

[40] M. Lerch, Nitridation of Zirconia, J. Am. Ceram. Soc. 79 (1996) 2641–2644, https://doi.org/10.1111/j.1151-2916.1996.tb09028.x.

[41] Y.-K. Paek, J.-H. Ahn, G.-H. Kim, S.-J.L. Kang, Effect of Nitrogen Atmosphere on the Densification of a 3-mol%-Yttria-Doped Zirconia, J. Am. Ceram. Soc. 85 (2002) 1631–1633, https://doi.org/10.1111/j.1151-2916.2002.tb00327.x.

[42] N. Claussen, R. Wagner, L.J. Gauckler, G. Petzow, Nitride-Stabilized Cubic Zirconia, J. Am. Ceram. Soc. 61 (1978) 369–370, https://doi.org/10.1111/j.1151-2916.1978.tb09333.x.

[43] Y. Cheng, D.P. Thompson, Nitrogen-Containing Tetragonal Zirconia, J. Am. Ceram. Soc. 74 (1991) 1135–1138, https://doi.org/10.1111/j.1151-2916.1991.tb04355.x.

[44] Y.-B. Cheng, D.P. Thompson, Role of Anion Vacancies in Nitrogen-Stabilized Zirconia, J. Am. Ceram. Soc. 76 (1993) 683–688, https://doi.org/10.1111/j.1151-2916.1993.tb03660.x.

[45] T.-J. Chung, J.-S. Lee, D.-Y. Kim, H. Song, Surface Nitridation of Yttria-Doped Tetragonal Zirconia Polycrystals (Y-TZP): Microstructural Evolution and Kinetics, J. Am. Ceram. Soc. 82 (1999) 3193–3199, https://doi.org/10.1111/j.1151-2916.1999.tb02223.x.

[46] T.-J. Chung, J.-S. Lee, D.-Y. Kim, G.-H. Kim, H. Song, Morphology and Phase Stability of Nitrogen–Partially Stabilized Zirconia (N-PSZ), J. Am. Ceram. Soc. 84 (2001) 172–178, https://doi.org/10.1111/j.1151-2916.2001.tb00626.x.

[47] A. Feder, J. Alcalá, L. Llanes, M. Anglada, Microstructure, mechanical properties and stability of nitrided Y-TZP, J. Eur. Ceram. Soc. 23 (2003) 2955–2962, https://doi.org/10.1016/S0955-2219(03)00307-8.

[48] R. Milani, R.P. Cardoso, T. Belmonte, C.A. Figueroa, C.A. Perottoni, J.E. Zorzi, G. V. Soares, I.J.R. Baumvol, Nitriding of yttria-stabilized zirconia in atmospheric pressure microwave plasma, J. Mater. Res 24 (2009) 2021–2028, https://doi.org/10.1557/jmr.2009.0245.

[49] Y.P. Kathuria, Laser surface nitriding of yttria stabilized tetragonal zirconia, Surf. Coat. Technol. 201 (2007) 5865–5869, https://doi.org/10.1016/j.surfcoat.2006.10.041.

[50] T. Kurachi, Y. Yamashita, T. Tokunaga, H. Yoshida, T. Yamamoto, Suppression of nitridation of yttria-doped zirconia during flash sintering, J. Am. Ceram. Soc. 103 (2020) 3002–3007, https://doi.org/10.1111/jace.16990.

[51] R.F. Walker, Mechanism of Material Transport During Sintering, J. Am. Ceram. Soc. 38 (1955) 187–197, https://doi.org/10.1111/j.1151-2916.1955.tb14928.x.

[52] R.L. Coble, Sintering Alumina: Effect of Atmospheres, J. Am. Ceram. Soc. 45 (1962) 123–127, https://doi.org/10.1111/j.1151-2916.1962.tb11099.x.

[53] S.K. Roy, Effects of Atmosphere on Sintering of Alumina, Trans. Indian Ceram. Soc. 54 (1995) 190–196, https://doi.org/10.1080/0371750X.1995.10804718.

[54] S.-J.L. Kang, What we should consider for full densification when sintering, Materials 13 (2020) 3578, https://doi.org/10.3390/ma13163578.

[55] A.F.S. Marques, F.A.P. Loureiro, N. Sahoo, J.R.O.F. Marques, M.F.B. da Cruz, A.D.S. P. da Mata, J. Caramês, F.S.C.P. da Silva, Ó.S.N. Carvalho, Nd-YAG Laser Texturing of Zirconia Implant Surfaces, Lasers Manuf. Mater. Process. 10 (2023) 1–18, https://doi.org/10.1007/s40516-022-00191-5.

[56] M. Bortolotti, L. Lutterotti, G. Pepponi, Combining XRD and XRF analysis in one Rietveld-like fitting, Powder Diffr. 32 (2017) S225–S230, https://doi.org/10.1017/S0885715617000276.
[57] W. Bao, S. Robertson, J.-X. Liu, G.-J. Zhang, F. Xu, H. Wu, Structural integrity and characteristics at lattice and nanometre levels of ZrN polycrystalline irradiated by 4 MeV Au ions, J. Eur. Ceram. Soc. 38 (2018) 4373–4383, https://doi.org/10.1016/j.jeurceramsoc.2018.05.013.
[58] C. Bechteler, R.I. Todd, Lattice modification of $ZrO_{2-\delta}$ and formation of rocksalt structure ZrO and Zr(O,N) after DC electrical loading of 3YSZ, J. Eur. Ceram. Soc. (2023), https://doi.org/10.1016/j.jeurceramsoc.2023.09.014.
[59] A.P. Naumenko, N.I. Berezovska, M.M. Biliy, O.V. Shevchenko, Vibrational analysis and Raman spectra of tetragonal zirconia, Phys. Chem. Solid State 9 (2008) 121–125.
[60] J.-M. Costantini, G. Gutierrez, G. Lelong, M. Guillaumet, Md.M. Rahman, K. Yasuda, Raman spectroscopy study of damage in swift heavy ion-irradiated ceramics, J. Raman Spectrosc. 53 (2022) 1614–1624, https://doi.org/10.1002/jrs.6414.
[61] C. Bechteler, R.I. Todd, Investigation about the electrochemical reduction in 3YSZ, related phase transition and consequences, ArXiv Preprint ArXiv:2307.03557 (2023), https://doi.org/10.48550/arXiv.2307.03557.
[62] M. Biesuz, L. Pinter, T. Saunders, M. Reece, J. Binner, V.M. Sglavo, S. Grasso, Investigation of electrochemical, optical and thermal effects during flash sintering of 8YSZ, Materials 11 (2018) 1214, https://doi.org/10.3390/ma11071214.
[63] J. Janek, C. Korte, Electrochemical blackening of yttria-stabilized zirconia – morphological instability of the moving reaction front, Solid State Ion.-. 116 (1999) 181–195, https://doi.org/10.1016/S0167-2738(98)00415-9.
[64] C. Gionco, M.C. Paganini, E. Giamello, R. Burgess, C. Di Valentin, G. Pacchioni, Paramagnetic Defects in Polycrystalline Zirconia: An EPR and DFT Study, Chem. Mater. 25 (2013) 2243–2253, https://doi.org/10.1021/cm400728j.
[65] N. Morisaki, H. Yoshida, K. Matsui, T. Tokunaga, K. Sasaki, T. Yamamoto, Synthesis of zirconium oxynitride in air under DC electric fields, Appl. Phys. Lett. 109 (2016) 083104, https://doi.org/10.1063/1.4961624.
[66] I. Milošev, H.-H. Strehblow, M. Gaberšček, B. Navinšek, Electrochemical Oxidation of ZrN Hard (PVD) Coatings Studied by XPS, Surf. Interface Anal. 24 (1996) 448–458, https://doi.org/10.1002/(SICI)1096-9918(199607)24:7%3C448::AID-SIA137%3E3.0.CO;2-F.
[67] P. Carvalho, J.M. Chappé, L. Cunha, S. Lanceros-Méndez, P. Alpuim, F. Vaz, E. Alves, C. Rousselot, J.P. Espinós, A.R. González-Elipe, Influence of the chemical and electronic structure on the electrical behavior of zirconium oxynitride films, J. Appl. Phys. 103 (2008) 104907, https://doi.org/10.1063/1.2927494.
[68] D. Majumdar, D. Chatterjee, X-ray photoelectron spectroscopic studies on yttria, zirconia, and yttria-stabilized zirconia, J. Appl. Phys. 70 (1991) 988–992, https://doi.org/10.1063/1.349611.
[69] I. Takano, S. Isobe, T.A. Sasaki, Y. Baba, Nitrogenation of various transition metals by N+2-ion implantation, Appl. Surf. Sci. 37 (1989) 25–32, https://doi.org/10.1016/0169-4332(89)90970-7.
[70] D. Hauser, A. Auer, J. Kunze-Liebhäuser, S. Schwarz, J. Bernardi, S. Penner, Hybrid synthesis of zirconium oxycarbide nanopowders with defined and controlled composition, RSC Adv. 9 (2019) 3151–3156, https://doi.org/10.1039/C8RA09584A.
[71] D. Hauser, C. Grießer, E.-M. Wernig, T. Götsch, J. Bernardi, J. Kunze-Liebhäuser, S. Penner, The pervasive presence of oxygen in ZrC, Surf. Interfaces 34 (2022) 102373, https://doi.org/10.1016/j.surfin.2022.102373.
[72] M. Kleitz, L. Dessemond, M.C. Steil, Model for ion-blocking at internal interfaces in zirconias, Solid State Ion.-. 75 (1995) 107–115, https://doi.org/10.1016/0167-2738(94)00143-G.
[73] M.C. Steil, F. Thevenot, M. Kleitz, Densification of yttria-stabilized zirconia: impedance spectroscopy analysis, J. Electrochem Soc. 144 (1997) 390, https://doi.org/10.1149/1.1837416.
[74] J.-C. M'Peko, J.S.C. Francis, R. Raj, Impedance Spectroscopy and Dielectric Properties of Flash Versus Conventionally Sintered Yttria-Doped Zirconia Electroceramics Viewed at the Microstructural Level, J. Am. Ceram. Soc. 96 (2013) 3760–3767, https://doi.org/10.1111/jace.12567.
[75] M. Levy, J. Fouletier, M. Kleitz, Model for the electrical conductivity of reduced stabilized zirconia, J. Electrochem Soc. 135 (1988) 1584, https://doi.org/10.1149/1.2096057.
[76] M. Biesuz, L. Karacasulu, C. Vakifahmetoglu, V.M. Sglavo, On the temperature measurement during ultrafast high-temperature sintering (UHS): Shall we trust metal-shielded thermocouples? J. Eur. Ceram. Soc. 44 (2024) 3479–3485, https://doi.org/10.1016/j.jeurceramsoc.2023.11.061.
[77] J.A. Krogstad, M. Lepple, Y. Gao, D.M. Lipkin, C.G. Levi, Effect of Yttria Content on the Zirconia Unit Cell Parameters, J. Am. Ceram. Soc. 94 (2011) 4548–4555, https://doi.org/10.1111/j.1551-2916.2011.04862.x.
[78] P. Vult von Steyern, E. Bruzell, L. Vos, F.S. Andersen, A. Ruud, Sintering temperature accuracy and its effect on translucent yttria-stabilized zirconia: Flexural strength, crystal structure, tetragonality and light transmission, Dent. Mater. 38 (2022) 1099–1107, https://doi.org/10.1016/j.dental.2022.04.023.
[79] C.-J. Ho, W.-H. Tuan, Phase stability and microstructure evolution of yttria-stabilized zirconia during firing in a reducing atmosphere, Ceram. Int 37 (2011) 1401–1407, https://doi.org/10.1016/j.ceramint.2011.01.008.
[80] M.J. Balart, J.B. Patel, F. Gao, Z. Fan, Grain Refinement of Deoxidized Copper, Metall. Mater. Trans. A 47 (2016) 4988–5011, https://doi.org/10.1007/s11661-016-3671-8.
[81] R. Marchand, Y. Laurent, J. Guyader, P. L'Haridon, P. Verdier, Nitrides and oxynitrides: Preparation, crystal chemistry and properties, J. Eur. Ceram. Soc. 8 (1991) 197–213, https://doi.org/10.1016/0955-2219(91)90096-I.
[82] I. Barin. Thermochemical Data of Pure Substances, VCH Verlagsgesellschaft mbH, Weinheim, 1995, https://doi.org/10.1002/9783527619825.ch7.
[83] I. Valov, V. Rührup, R. Klein, T.-C. Rödel, A. Stork, S. Berendts, M. Dogan, H.-D. Wiemhöfer, M. Lerch, J. Janek, Ionic and electronic conductivity of nitrogen-doped YSZ single crystals, Solid State Ion.-. 180 (2009) 1463–1470, https://doi.org/10.1016/j.ssi.2009.09.003.
[84] S.-W. Kim, S.G. Kim, J.-I. Jung, S.-J.L. Kang, I.-W. Chen, Enhanced Grain Boundary Mobility in Yttria-Stabilized Cubic Zirconia under an Electric Current, J. Am. Ceram. Soc. 94 (2011) 4231–4238, https://doi.org/10.1111/j.1551-2916.2011.04800.x.
[85] Y. Dong, H. Wang, I.-W. Chen, Electrical and hydrogen reduction enhances kinetics in doped zirconia and ceria: I. grain growth study, J. Am. Ceram. Soc. 100 (2017) 876–886, https://doi.org/10.1111/jace.14615.
[86] Y. Dong, I.-W. Chen, Electrical and hydrogen reduction enhances kinetics in doped zirconia and ceria: II. Mapping electrode polarization and vacancy condensation in YSZ, J. Am. Ceram. Soc. 101 (2018) 1058–1073, https://doi.org/10.1111/jace.15274.
[87] Y. Dong, L. Qi, A. Alvarez, J. Li, I.-W. Chen, Enhanced mobility of cations and anions in the redox state: The polaronium mechanism, Acta Mater. 232 (2022) 117941, https://doi.org/10.1016/j.actamat.2022.117941.
[88] Y. Dong, Redox enhanced slow ion kinetics in oxide ceramics, J. Am. Ceram. Soc. 107 (2024) 1905–1916, https://doi.org/10.1111/jace.19441.
[89] E. Martin, U.C. Chung, M. Duttine, M.A. Dourges, G. Clermont, C. Labrugère, S. Fourcade, D. Michau, C. Estournès, T. Hérisson de Beauvoir, F. Mauvy, V. Jubera, M. Maglione, G. Goglio, C. Elissalde, Defect chemistry to trigger zirconia densification at low temperatures by Spark Plasma Sintering, Open Ceram. 17 (2024) 100518, https://doi.org/10.1016/j.oceram.2023.100518.